AIAA 2013-2517

Numerical Simulation of Pitching Airfoil Performance Enhancement Using Co-Flow Jet Flow Control

Alexis Lefebvre*, G.-C. Zha†
Dept. of Mechanical and Aerospace Engineering
University of Miami
Coral Gables, Florida 33124
E-mail: gzha@miami.edu

Abstract

The two dimensional flow of an oscillating SC1095 airfoil with Co-Flow Jet (CFJ) flow control is simulated using Unsteady Reynolds Average Navier-Stokes (URANS). A 5th order WENO scheme for the inviscid flux, a 4th order central differencing model for the viscous terms and the one equation Spalart-Allmaras model for the turbulence are used to resolve the flow. The Mach number is 0.3 and Reynolds number is 3.93×10^6 at reduced frequency from 0.05 to 0.2. The simulated results for the baseline agree reasonably well with the experiments for no-stall, mild-stall and deep-stall cases. The CFJ pitching airfoil is found to increase the airfoil performance for every flow studied. At $C_\mu = 0.08$ the lift is increased by 32% and the drag is decrease by 80%. Considering only the aerodynamic forces applied on the airfoil and not the pumping power, $(L/D)_{ave}$ for this case reach an outstanding 118.3. When C_μ is increased, the average drag becomes negative, proving the feasibility of a CFJ helicopter blade using its pump as the only source of power. Due to the removal of dynamic stall, CFJ airfoil is able to remove the sharp moment drop at high angle of attack.

Nomenclature

CFJ	Co-flow jet
AoA	Angle of attack
LE	Leading Edge
TE	Trailing Edge
$ZNMF$	Zero-net mass-flux
S	Planform area
c	Profile chord
U	Flow velocity
q	Dynamic pressure $0.5\,\rho\,U^2$
p	Static pressure
ρ	Air density
ω	Angular velocity of oscillation
$\dot{m}$	Mass flow
M	Mach number
∞	Free stream conditions
j	Jet conditions
α_0	Mean angle of attack

* Graduate Student, AIAA Member
† Associate Professor, AIAA Senior Member

α_1	Amplitude of oscillation
k	Reduced frequency $\omega\, c/(2\, U_\infty)$
τ	Dimensionless time $2\, t\, U_\infty/c$
t	Real time
C_L	Lift coefficient $L/(q_\infty\, S)$
C_D	Drag coefficient $D/(q_\infty\, S)$
C_p	Pressure coefficient $(p - p_\infty)/q$
C_μ	Jet momentum coef. $\dot{m}_j\, U_j/(q\, S)$

1 Introduction

1.1 State of the Art Overview

The forward moving helicopter blades undergo a sinusoidal movement in order to achieve the balance of lift between advancing and retreating side of the rotor disk. The AoA is minimum for the advancing blade while the retreating blade must increase the AoA in order to keep the balance of force. This unsteady motion allows higher AoA than the static stall angle.

The physics of the dynamic stall is well documented by Bousman [1] in his study include a level flight case at high altitude, a diving turn at high load factor, and the UTTAS pull-up maneuver. The dynamic stall is much alike for all of these flight conditions characterized by the shedding of a vortex at a near leading edge (LE) position both in simulation and in two-dimensional wind tunnel testing. Similar observation are done by McCroskey et al. [2] who concluded that dynamic stall come from the breakdown of a turbulent boundary layer as opposed to the burst of a laminar separation bubble.As the dynamic vortex is created, the blade experiences a peak performance in term of lift, drag and momentum. However, as the vortex structures move downward, the performance collapse resulting in a hysteresis loop behavior for forces and moment. The sudden down-nose momentum peak submits the blade to sever torsion that lead to fatigue and failure problems [3], and severely impair the maneuverability of the aircraft [1].

In order to extend the flight envelop of rotor craft, research has been done to mitigate the dynamic stall. Early studies show that modifying the airfoil profile alone [4, 5] could improve slightly the performance during a light stall but have limited effect on the deep-stall. This suggests that more radical solution have to be found to remove the dynamic stall. One of the method is to introduce slat in the blade design. McAlister et al. [6] studied experimentally the VR-7 slatted airfoil for a range of AoA. The slat configuration is able to minimize the lift collapse due to dynamic stall and to effectively smooth the momentum coefficient. Reynolds number shows little influence on the slat effect. However the slatted configuration is found to have only moderate increase in average L/D over the cycle and maximum drag reaches a value well above 0.3 at large AoA.

In a more recent study Mishra [7] showed the effect of 2 slats configurations on the dynamic stall on rotor blade UH60A aerodynamic and dynamic response. His results confirm the static slat effectiveness in reducing forces hysteresis during dynamic stall and smoothing the momentum coefficient. Dynamic slats are not found to generate better results than the static slat configuration.

Yee et al. [8] studied the aerodynamic characteristics of the Gurney flap using 2D simulation for various Mach number and flap height. They found that a 2% height Gurney flap increases the effective camber and nose-down momentum of the airfoil. The performance is slightly increased in the light stall but no substantial improvement is found for the deep-stall case.

Thakkar et al. [9] explored a new single-crystal piezoceramic for its potential to torsionally actuate the elastic rotor blade utilizing the induced shear mechanism of piezoceramics. Their numerical study

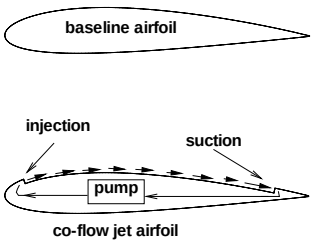

Figure 1: CFJ airfoil concept

shows a possible reduction of the AoA by up to 8.7°, which suggests the possibility to dynamically twist the blade to suppress the dynamic stall. However performance improvements are yet to be quantified.

Another promising study have been done by Sun et al. [10] in their numerical study of tangential jet effect on dynamic stall using RANS equations using Baldwin-Lomax turbulence model. Their study focused on a pitching motion of a NACA0012 with oscillating with 10° amplitude about a 15° mean angle at a reduced frequency in the range 0.15-0.25. They were able to mitigate the stall at $C_\mu = 0.7$ using steady jets. They also found that using unsteady jets with strength periodically varying with the wing cycle is more effective at reducing the dynamic stall. Also jet position at about 0.6% chord location is found to be more effective than a more downstream position. However their results are more qualitative than quantitative due to the lack of precision when resolving large separated flow.

1.2 Co-Flow Jet (CFJ) Flow Control Airfoil

Recently, a zero-net mass-flux (ZNMF) co-flow jet flow control airfoil developed by Zha et al. [11, 12, 13, 14, 15, 16, 17] based on fluidic actuators is demonstrated to achieve radical lift augmentation, stall margin increase, and drag reduction for stationary airfoil due to its high control authority.

In the CFJ airfoil concept [12, 11, 13, 14, 15, 16, 17], an injection slot near leading edge (LE) and a suction slot near trailing edge (TE) on the airfoil suction surface are created as sketched in Fig. 1. A small amount of mass flow is withdrawn into the airfoil near the TE, pressurized and energized by a pumping system inside the airfoil, and then injected near the LE in the direction tangent to the main flow. The whole process does not add any mass flow to the system and hence is a ZNMF flow control. The energy expenditure is low [12, 17] and the implementation is straightforward.

The purpose of this paper is to make the first effort to apply CFJ airfoil to pitching airfoil using numerical simulation as a proof of concept. The goal of CFJ pitching airfoil is to remove dynamic stall in the typical pitching airfoil working range with drastic enhancement of maximum lift and drag reduction.

2 Numerical Simulations Overview

2.1 CFD Code

The FASIP (Flow-Acoustics-Structure Interaction Package) CFD code is used to conduct the numerical simulation. The 2D Reynolds averaged Navier-Stokes (RANS) equations with one-equation Spalart-Allmaras [18] turbulence model is used. A 5th order WENO scheme for the inviscid flux [19, 20, 21, 22, 23, 24, 25] and a 4th order central differencing for the viscous terms [19, 24] are employed

to discretize the Navier-Stokes equations. The low diffusion E-CUSP scheme used as the approximate Riemann solver suggested by Zha et al [20] is utilized with the WENO scheme to evaluate the inviscid fluxes. Implicit time marching method using Gauss-Seidel line relaxation is used to achieve fast convergence rate[26]. Parallel computing is implemented to save wall clock simulation time[27]. The RANS solver is validated for CFJ static airfoil simulation [15].

2.2 Mesh

The computation mesh is constructed using the O-mesh topology in order to achieve high quality around the airfoil. The CFJ SC1095 airfoil mesh displayed Fig. 2 uses a total of 360 points placed around airfoil partitioned into 240 points on suction surface and 120 points on the pressure surface. 180 points are placed in the direction normal to the airfoil with an additional 50 points across the jet. Total mesh size is 77,800 cells, partitioned into 23 blocks for the parallel computation. The farfield boundary is located 50 chords away from the airfoil. To resolve the turbulent boundary layer, the first grid point is placed at $y^+ \approx 0.5$. The baseline airfoil mesh is constructed using the same strategy. The total baseline airfoil mesh size is 54,000 cells with 271 points around the airfoil and 181 points normal to the airfoil. The baseline airfoil mesh is split into 9 blocks for the parallel computing. For both baseline airfoil and CFJ airfoil, a refined grid is constructed using 50% more points in every direction and $y^+ \approx 0.35$.

2.3 Boundary Conditions

The wall treatment suggested in [23] to achieve the flux conservation on the wall is employed. The 3rd order accuracy no slip condition is enforced on the solid surface as described in Ref. [23]. Total pressure, total temperature and flow angle are specified as the inlet boundary conditions for the upstream portion of the farfield boundary and inside the injection cavity. Constant static pressure is used downstream at the farfield boundary and in the suction cavity.

To achieve zero-net mass-flux with the CFJ flow control, the mass flow that exits the injection slot must equal the mass flow entering the suction slot. Additionally, the jet strength must be controlled in order to reach the prescribed C_μ. This is achieved by iterating the jet total pressure until the C_μ value is within 1% of the prescribed value. Total temperature is assumed constant during this process. At the suction cavity, the injection and suction mass flow are matched by iterating the static pressure at the suction cavity. The process is iterated throughout the simulation until the specified momentum coefficient is reached and the injection and suction mass flow match.

2.4 Cases description

The baseline airfoil SC1095 used on the UH-60 Black Hawk US-army helicopter is chosen due to the existence of experimental data from NASA [5]. CFJ is implemented on the SC1095 profile via multiple geometries depicted in Table 1. For most cases geometry 1 performs well. However for a high C_μ, a bigger jet slot is used in order to keep the jet exit Mach number within acceptable range. A bigger suction slot is also used to suck in the increasing mass flow.

Mach number of 0.3 and Reynolds number of 3.93×10^6 at reduced frequency from 0.05 to 0.2 are used to match the experimental data. The CFJ airfoil uses the same conditions with C_μ in the range of 0.08-0.24. The pitching motion for both baseline airfoil and CFJ airfoil is described by

$$AoA = \alpha_0 + \alpha_1 \, sin(k\,\tau)$$

From the no-stall case to the deep-stall case, the maximum AoA is increased from 14° to 19.68°. The parameters of the cases studied are given Table 2.

Geometry	Inj. slot height	Inj. slot location	Suc. slot height	Suc. slot location
1	0.50	5	0.75	80
2	0.75	5	1.12	70
3	1.00	5	1.50	70

Table 1: Description of the different geometries for deep-stall study, length are given in % of chord.

Case name	α_0 (°)	α_1 (°)	k
no-stall	3.88	10.11	0.15
mild-stall	9.93	4.91	0.05
deep-stall	9.78	9.90	0.10

Table 2: Pitching airfoil motion description.

3 Results

3.1 No-stall Case Baseline and CFJ results

Fig. 3 shows the computed baseline results for C_l, C_d and C_m compared with the experimental data. Good agreement exists between the lift and drag at lower AoA. At high AoA the prediction under-estimates the magnitude of both lift and drag with a 12% difference for the peak C_l and 20% difference for the peak C_d. The moment is slighlty overpredicted by the the computation. Those uncertainity are somewhat higher than the measurement uncertainty [5]. Time refinement study was perfomed by decreasing the unsteady time step by a factor 2. The results show perfect agreement with the baseline time step size, and indicate that the solution is converged based on time step size. Spatial mesh refinement is performed as indicated in the mesh section. The refined mesh shows overall the same results as the baseline mesh.

Fig. 4 shows the CFJ pitching airfoil C_l, C_d and C_m during the oscillation cycle at $C\mu = 0.08$. The maximum C_l increased from roughly 1.4 for the baseline airfoil to almost 1.8 for the CFJ airfoil. The C_d is decreased and remain negative during part of the plunging motion. The C_m variation is smooth.

3.2 Baseline Pitching Airfoil During Mild-Stall Case

Fig. 5 shows the baseline SC1095 pitching profile instantaneous Mach contour with streamlines at different AoA for the mild-stall case. The dynamic stall process is well captured with the flow attached at low AoA and a large separation moving dynamically at high AoA. The stall originates from the TE of the pitching airfoil.

Fig. 6 shows the computed baseline results for C_l, C_d and C_m compared with the experimental data. Similarly to previous case, good agreement exists between the data at lower AoA. However the lift is once again under-predicted at high AoA with a difference of 5% for the peak value, which is within the measurement uncertainty [5]. Also stall shape predition varies. It appears that the 2D URANS model does not capture accurately the complicated turbulence during dynamic stall and predicts a sharper stall. The moment coefficient is in good agreament except for the over-estimated peak value. The drag prediction is in good agreement with a slight under-prediction at low AoA and a peak value that matches the experiments. Time refinement study was perfomed by decreasing the unsteady time step by a factor of 2. The results show an excellent agreement with the baseline time step. The spatial mesh refinement basically gives the same results with a slight improvement.

3.3 CFJ Pitching Airfoil During Mild-Stall Case

Fig. 7 shows the CFJ SC1095 pitching airfoil instantaneous Mach contour with streamlines at different AoA for the mild-stall case with $C_\mu = 0.08$. A zoomed in picture of the injection and suction region are added. Those regions use their own scale defined in the header of the plot. The CFJ completely removes the dynamic stall for the mild-stall case at relatively low C_μ. The LE suction surface peak velocity reaches $M \approx 0.7$, greater than the baseline peak velocity of $M \approx 0.6$.

Fig. 8 shows the CFJ pitching airfoil C_l, C_d and C_m during the oscillation cycle at $C\mu = 0.08$. The CFJ pitching airfoil reaches an increase of lift by up to a factor of 2.2 with an associated drag reduction by a factor of 6.2. The drag is negative during most of the pitching motion and remains very low otherwise.

The top of Fig. 9 shows the injection and suction mass flow during the pitching motion. The mean injection mass flow is $M_{inj} = 0.0137$ while the mean suction mass flow is $M_{suc} = 0.0134$ which is a 2.2% difference. Due to the pitching oscillation, the static pressure of the main flow at CFJ injection location also oscillates with the AoA. To maintain a constant injection mass flow rate, the injection total pressure hence needs to be oscillating as shown in the bottom of Fig. 9. At high AoA, the suction surface pressure behind the airfoil LE is lower, hence a lower injection total pressure is needed to maintain a constant injection mass flow rate. At low AoA, the suction surface pressure behind LE is higher, a higher injection total pressure is used to achieve the same mass flow rate.

The bottom of Fig. 9 shows the oscillation of the suction cavity static pressure and mass flow. At low AoA, a lower suction pumping power is required due to the high jet momentum at the suction slot. In consequence the suction cavity static pressure remains relatively high. At large AoA, the LE wake size increases and an increasing share of the jet momentum is used to re-energize the wake. The available jet momentum at the suction slot decreases and a lower suction cavity static pressure is used to keep the mass flow steady. At the end of the pitching motion, deprived of the incoming jet momentum, the suction slot fails for a brief instant to suck in the required mass flow.

At high AoA, lowering further the suction cavity pressure had little effect on the suction mass flow. This suggest other solutions have to be implemented to keep the suction mass flow steady. Those solutions include reducing the LE wake by modifying the airfoil profile and/or put the injection slot at more aft position. Using a variable geometry suction slot that would open up the suction slot when more pumping power is required. Finally using of a buffer zone inside the injection or suction cavities to allow the CFJ airfoil to work properly with a brief difference between injection and suction mass flow.

Fig. 10 shows the computed C_p coefficient on the wall for the baseline and the CFJ profile. A jump occurs at the injection and suction slots as the C_p is measured on discontinuous wall surfaces. The suction surface loading is significantly higher than the baseline airfoil, which gives a higher lift.

3.4 Baseline Pitching Airfoil During Deep-Stall Case

Fig. 11 shows the baseline SC1095 pitching airfoil instantaneous Mach contour with streamlines at different AoA for the deep-stall case. It clearly exhibits a massive separation that originates from the LE and moves to the TE. Compared with the mild-stall case, the flow separation inception location differs and the separation region is significantly larger due to the higher AoA of oscillation.

Fig. 12 shows the computed baseline results for C_l, C_d and C_m compared with the experimental data. Fairly good agreement is obtained between computation and experiment. The numerical simulation tends to stall slightly earlier by about 1° and in a sharper manner than the experiments. The peak lift is slightly under-predicted but remains within the measurement uncertainty [5]. The mesh and time refinement results agree very well with the baseline mesh and time step with some slight difference in the stall region of the pitching motion. When compared with 2D calculations from other research

laboratories, the results displayed show some improvement on the overall forces predictions [28].

3.5 CFJ Pitching Airfoil During Deep-Stall Case

To study the CFJ effect of the deep-stall case, 3 CFJ geometries are created as seen in Table 1. The $C_\mu = 0.08$ albeit beneficial for the mild-stall case, fails to remove the deep-stall. For this reason higher C_μ are selected depending on the geometry slot size.

Fig. 13, 14 and 15 show the instantaneous Mach contour of the CFJ SC1095 geometry 1, 2 and 3 with streamlines at different AoA and $C\mu$ for the deep-stall case. A zoomed in picture of the injection and suction region are added. Those regions use their own scale defined in the header of the plot.

Geometry 1 strongly mitigate the deep-stall negative effects at $C_\mu = 0.12$. Fig. 16 shows the dynamic stall that occurs only during a limited range of AoA. At high AoA, the large adverse pressure gradient at the LE creates a localized micro-recirculation. At $AoA = 18.50°$ the LE micro-recirculation and its associated wake reach their peak size. The jet is too weak to re-energize the low speed wake flow and a recirculation region develops close to the TE of the wing. At $AoA = 19.52°$ the TE micro-recirculation recedes and the flow reattaches. The abrupt change of C_p seen at the bottom of Fig. 16 coincides with the growth and burst of the LE micro-recirculation. The LE suction surface peak velocity reaches $M \approx 0.8$, greater than the baseline peak velocity of $M \approx 0.6$. Interestingly the low ambient pressure above the jet exit slot at large AoA allows the supersonic jet to expand and to reach higher velocity than the jet exit. Low supersonic jets are more costly to produce than subsonic jets, but they carry extra momentum that is beneficial from a performance point of view. However achieving jet velocity above roughly $M = 2.0$ is expected to trigger strong lambda shock wave and to create an earlier stall as seen in previous steady airfoil study [29].

Geometry 2 and geometry 3 completely remove the dynamic stall at values of $C_\mu = 0.20$ and $C_\mu = 0.24$ respectively. The size of the jet slot shows no influence on the LE micro-recirculation size. The larger jet slot high of geometry 3 allow to reach higher C_μ at a relatively low jet velocity. This makes the geometry 3 jet more cost effective at similar C_μ than geometry 2. The LE suction surface peak velocity reaches $M \approx 1.0$.

Fig. 17 shows the CFJ pitching airfoil C_l, C_d and C_m during the oscillation cycle for geometry 1, 2 and 3. Each geometry uses a different $C\mu$ depending on the jet exit size. Geometry 1 mitigate the dynamic stall negative effects and provide higher lift and reduced drag compared to the baseline pitching airfoil. The moment peak associated with the deep-stall remains contained which indicates that this flight regime would be acceptable from a mechanical and maneuverability point of view. Geometry 2 and 3 completely remove the dynamic stall and provide an increase of lift by up to a factor of 2.1 with an associated drag reduction by a factor of 6.0. The drag is negative during most of the pitching and plunging motion. There is no abrupt change of C_m during the pitching cycle.

Fig. 18 shows the computed C_p coefficient on the wall for the baseline and the different CFJ geometries. The injection and suction C_p jumps are more important due to the higher C_μ. Geometry 2 which features the highest jet exit pressure show the highest C_p jump. As the LE micro-recirculation is created, C_p increases. Once the micro-recirculation further develop C_p drops abruptly. This explains the C_l sharp peak just before the deep-stall as seen Fig. 12. The suction surface pressure is significantly lower than the baseline airfoil, which gives a higher lift.

4 Discussion

The summary of the aerodynamic performance for all the cases studied can be seen Table 3. All the data are time averaged. The CFJ airfoil increase significantly the aerodynamic performance in all the cases studies. For the deep-stall case using geometry 2 and $C\mu = 0.20$ the CFJ airfoil thrust overcome

the drag, proving the feasibility of a CFJ helicopter blade using its pump as the only source of power. In addition, CFJ airfoils reduce the variation of momuntum ΔCm during the pitching cycle, simplifying the rotor design and improving the maneuverability. Research to apply CFJ on pitching airfoil at free stream Mach number of 0.4 is currently done. Recently, high performance CFJ pitching airfoils have been design, which potentially could further improve the aerodynamic performance at very low energetic cost. A detailed analysis of those airfoils, including the power consumption will be presented in the near future.

5 Conclusion

CFJ is implemented on the SC1095 profile. An attached flow case, a mild-stall case and a deep-stall case are simulated to test the CFJ pitching airfoil capabilities for removing the dynamic stall and quantify the overall performance improvement.

The CFJ pitching airfoil can remove the mild-stall using relatively low energy jets at $C_\mu = 0.08$. The deep-stall was strongly mitigated at $C_\mu = 0.12$ and completely removed at $C_\mu = 0.20$. The CFJ pitching airfoil is found to increase the airfoil performance for every flow studied. At $C_\mu = 0.08$ the lift is increased by 32% and the drag is decrease by 80%. Considering only the aerodynamic forces applied on the airfoil and not the pumping power, $(L/D)_{ave}$ for this case reach an outstanding 118.3. When C_μ is increased, the average drag becomes negative, proving the feasibility of a CFJ helicopter blade using its pump as the only source of power. Due to the removal of dynamic stall, CFJ airfoil is able to remove the sharp moment drop at high angle of attack. which is beneficial for blade material fatigue and maneuverability constraints.

The relatively sharp blade leading edge of the SC1095 airfoil creates a wake at high angle of attack that is found to be the main cause of jet momentum lost. Recently designed high performance CFJ pitching airfoils have shown have the potential to further improve the aerodynamic performance at very low energetic cost.

References

[1] William G. Bousman, "Airfoil Dynamic Stall and Rotorcraft Maneuverability." NASA/TM 2000-209601, AFDD/TR 00-A-008, 2000.

[2] W.J. McCroskey, L.W. Carr, and K.W. McAlister, "Dynamic Stall Experiments on Oscillating Airfoils." U.S. Army Air Mobility RnD Laboratory, Moffett Field, Calif., 1975.

[3] Prouty, R. W., "The Whys and Whats of Pitch-Link Loads." Rotor and Wing International, vol.22, no.10, 1988, pp 17-19.

[4] W.J. McCroskey, "Unsteady Airfoils." Fluid Mechanics, vol.14, 1982, pp 285-311.

[5] K. W. McAlister, S. L. Pucci, W. J. McCroskey and L. W. Carr, "An Experimental Study of Dynamic Stall on Advanced Airfoil Sections Volume 1. Summary of the Experiment." NASA TM 84245, 1982.

[6] K. W. McAlister and C. Tung, "Suppression of Dynamic Stall with a Leading-Edge Slat on a VR-7 Airfoil." NASA Technical Paper 3357, 1993.

[7] Asitav Mishra, "A Coupled CFD/CSD Investigation of the Effects of Leading Edge Slat on Rotor Performance." University of Maryland, Ph.D. thesis, 2012.

[8] Kwanjung Yee, Wandon Joo, and Dong-Ho Lee, "Aerodynamic Performance Analysis of a Gurney Flap for Rotorcraft Application." Journal of Aircraft, May, Vol. 44, No. 3 : pp. 1003-1014, 2007.

[9] D. Thakkar, R. Ganguli, "Single-crystal piezoceramic actuation for dynamic stall suppression." Sensors and Actuators, Volume 128, Issue 1, 2006.

[10] M. Sun, S. R. Sheikh, "Dynamic stall suppression on an oscillating airfoil by steady and unsteady tangential blowing." Aerospace Science and Technology, Volume 3, Issue 6, 1999.

[11] G.-C. Zha and D. C. Paxton, "A Novel Flow Control Method for Airfoil Performance Enhancement Using Co-Flow Jet." *Applications of Circulation Control Technologies*, Chapter 10, p. 293-314, Vol. 214, Progress in Astronautics and Aeronautics, AIAA Book Series, Editors: Joslin, R. D. and Jones, G.S., 2006.

[12] G.-C. Zha, W. Gao, and C. Paxton, "Jet Effects on Co-Flow Jet Airfoil Performance," *AIAA Journal, No. 6,*, vol. 45, pp. 1222–1231, 2007.

[13] G.-C. Zha, C. Paxton, A. Conley, A. Wells, and B. Carroll, "Effect of Injection Slot Size on High Performance Co-Flow Jet Airfoil," *AIAA Journal of Aircraft*, vol. 43, 2006.

[14] G.-C. Zha, B. Carroll, C. Paxton, A. Conley, and A. Wells, "High Performance Airfoil with Co-Flow Jet Flow Control," *AIAA Journal*, vol. 45, 2007.

[15] Wang, B.-Y. and Haddoukessouni, B. and Levy, J. and Zha, G.-C., "Numerical Investigations of Injection Slot Size Effect on the Performance of Co-Flow Jet Airfoil," *Journal of Aircraft*, vol. 45, No. 6, pp. 2084–2091, 2008,.

[16] B. P. E. Dano, D. Kirk, and G.-C. Zha, "Experimental Investigation of Jet Mixing Mechanism of Co- Flow Jet Airfoil." AIAA-2010-4421, 5th AIAA Flow Control Conference, Chicago, IL, 28 Jun - 1 Jul 2010.

[17] B. P. E. Dano, G.-C. Zha, and M. Castillo, "Experimental Study of Co-Flow Jet Airfoil Performance Enhancement Using Micro Discreet Jets." AIAA Paper 2011-0941, 49th AIAA Aerospace Sciences Meeting, Orlando, FL, 4-7 January 2011.

[18] P. Spalart and S. Allmaras, "A One-equation Turbulence Model for Aerodynamic Flows." AIAA-92-0439, 1992.

[19] Y.-Q. Shen and G.-C. Zha, "Large Eddy Simulation Using a New Set of Sixth Order Schemes for Compressible Viscous Terms ," *Journal of Computational Physics*, vol. 229, pp. 8296–8312, 2010.

[20] G.-C. Zha, Y. Shen, and B. Wang, "An improved low diffusion E-CUSP upwind scheme ," *Journal of Computer & Fluids*, vol. 48, pp. 214–220, 2011.

[21] Y.-Q. Shen and G.-Z. Zha , "Generalized finite compact difference scheme for shock/complex flowfield interaction," *Journal of Computational Physics*, vol. doi:10.1016/j.jcp.2011.01.039, 2011.

[22] Shen, Y.-Q. and Zha, G.-C. and Wang, B.-Y., " Improvement of Stability and Accuracy of Implicit WENO Scheme," *AIAA Journal*, vol. 47, No. 2, pp. 331–344, 2009.

[23] Y.-Q. Shen, G.-C. Zha, and B.-Y. Wang, "Improvement of Stability and Accuracy of Implicit WENO Scheme ," *AIAA Journal*, vol. 47, pp. 331–344, 2009.

[24] Shen, Y.-Q. and Zha, G.-C. and Chen, X.-Y., " High Order Conservative Differencing for Viscous Terms and the Application to Vortex-Induced Vibration Flows," *Journal of Computational Physics*, vol. 228(2), pp. 8283–8300, 2009.

[25] Shen, Y.-Q. and Zha, G.-C. , " Improvement of the WENO Scheme Smoothness Estimator," *International Journal for Numerical Methods in Fluids*, vol. DOI:10.1002/fld.2186, 2009.

[26] G.-C. Zha and E. Bilgen, "Numerical Study of Three-Dimensional Transonic Flows Using Unfactored Upwind-Relaxation Sweeping Algorithm," *Journal of Computational Physics*, vol. 125, pp. 425–433, 1996.

[27] B.-Y. Wang and G.-C. Zha, "A General Sub-Domain Boundary Mapping Procedure For Structured Grid CFD Parallel Computation," *AIAA Journal of Aerospace Computing, Information, and Communication*, vol. 5, No.11, pp. 2084–2091, 2008.

[28] Seongim Choi,Juan J. Alonso, Edwin v.d. Weide , "Validation Study of Aerodynamic Analysis Tools for Design Optimization of Helicopter Rotors," 2007.

[29] A. Lefebvre, B. Dano, M. D. Fronzo, W. B. Bartow, and G-C. Zha, "Performance of a Co-Flow Jet Airfoil with Variation of Mach Number," Jan 2013.

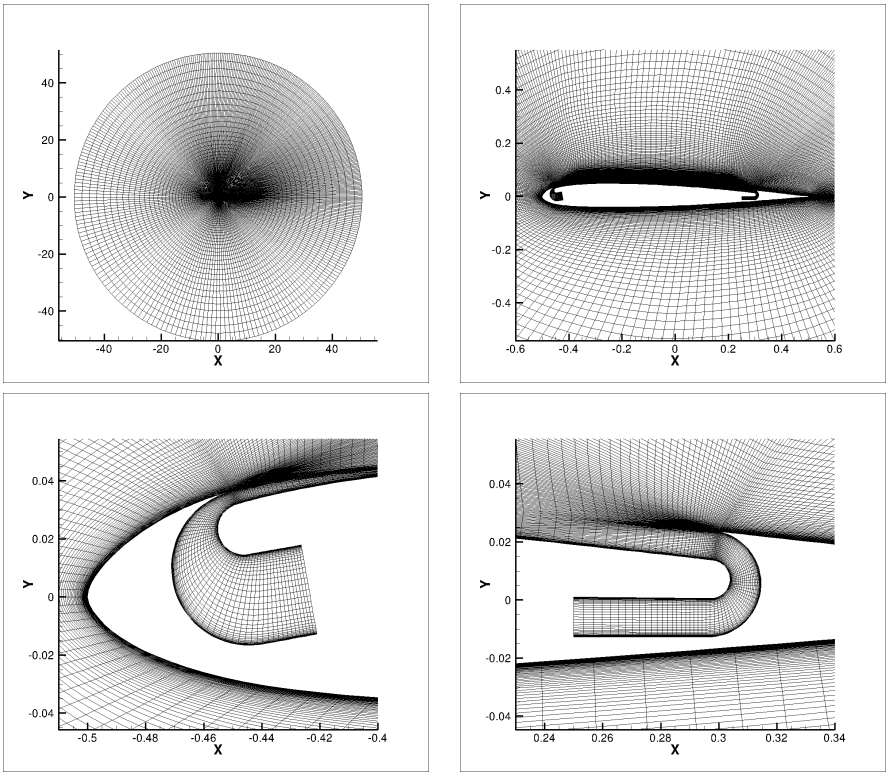

Figure 2: SC1095 CFJ pitching airfoil mesh topology.

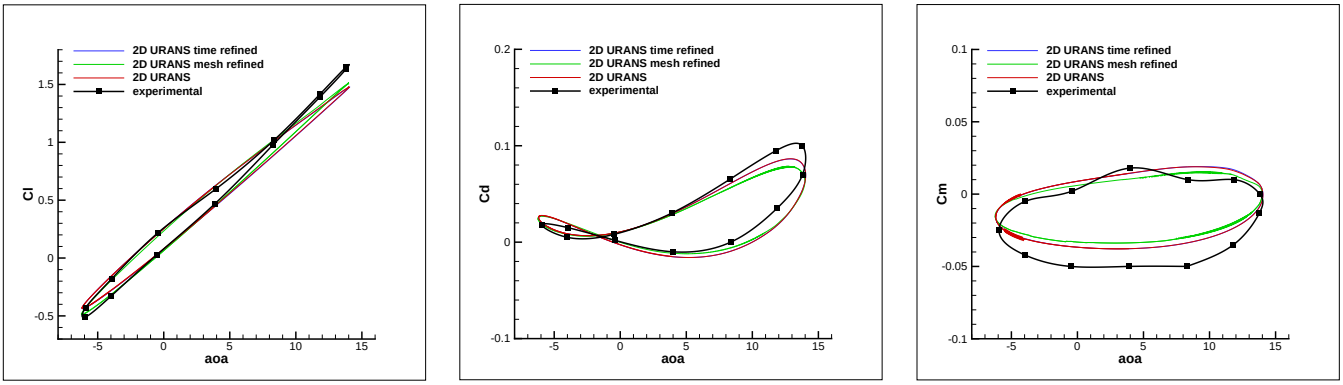

Figure 3: Baseline pitching airfoil C_l, C_d and C_m compared with experimental data during no-stall case.

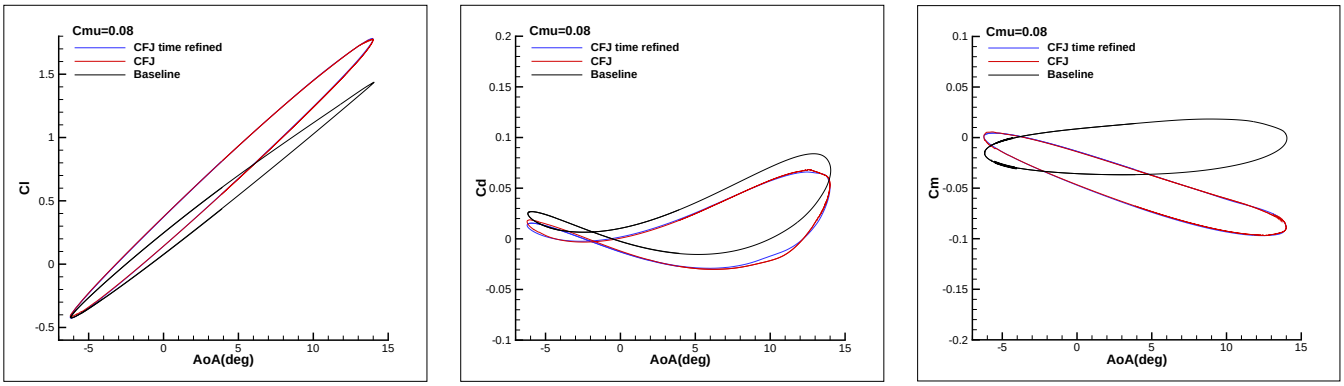

Figure 4: CFJ pitching airfoil C_l, C_d and C_m compared with baseline calculation during no-stall case.

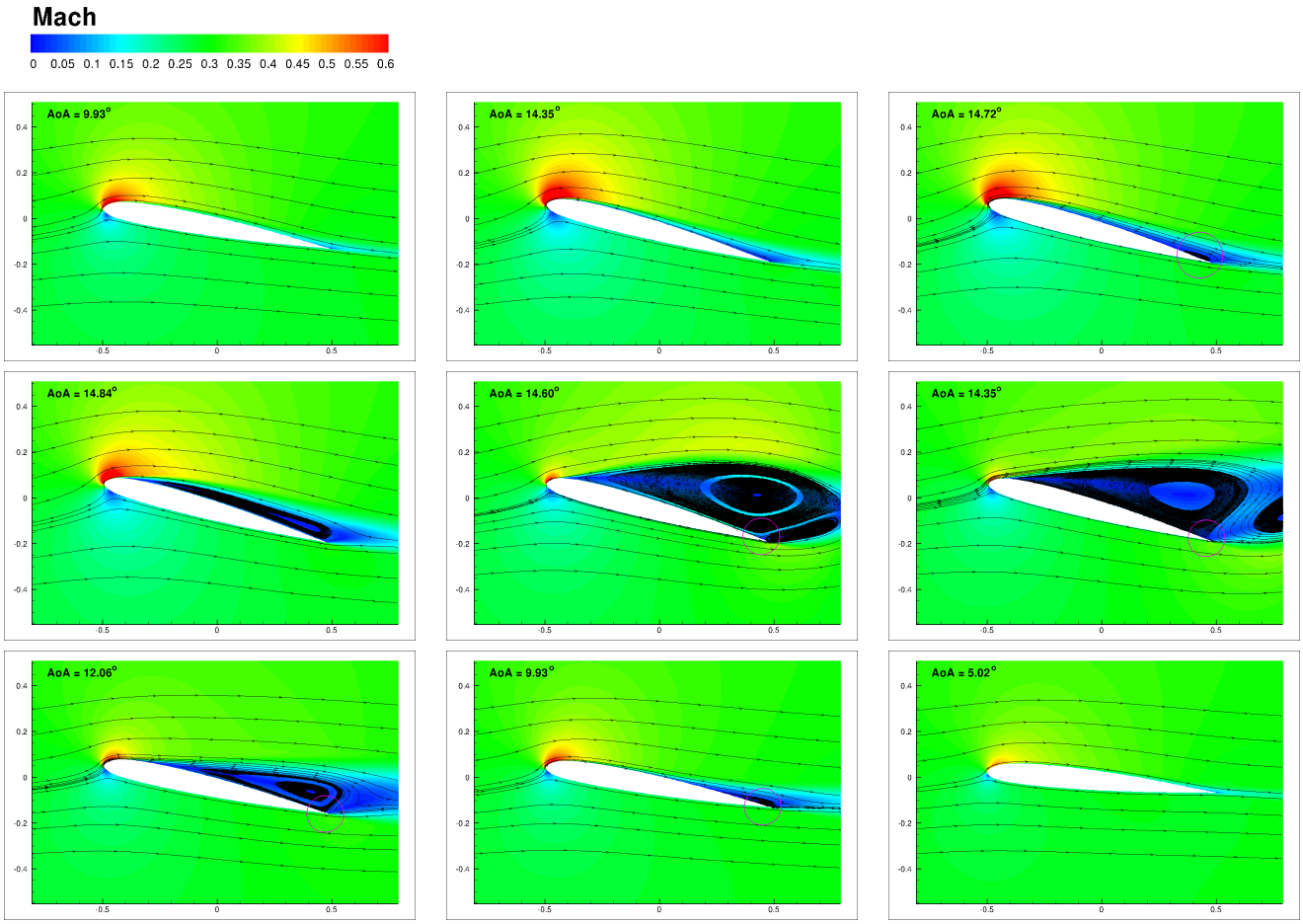

Figure 5: Instantaneous Mach contour of the baseline pitching airfoil with streamlines at different AoA for the mild-stall case.

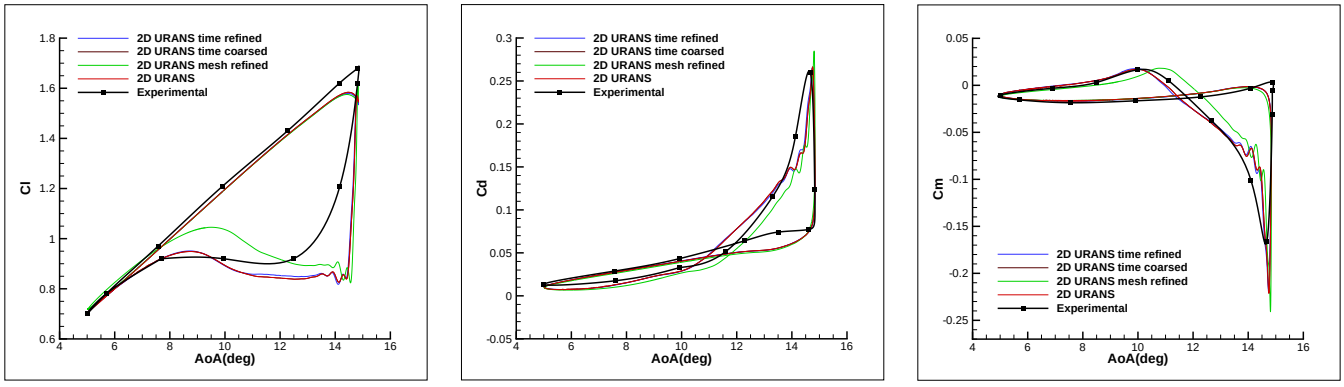

Figure 6: Baseline pitching airfoil C_l, C_d and C_m compared with experimental data during mild-stall case.

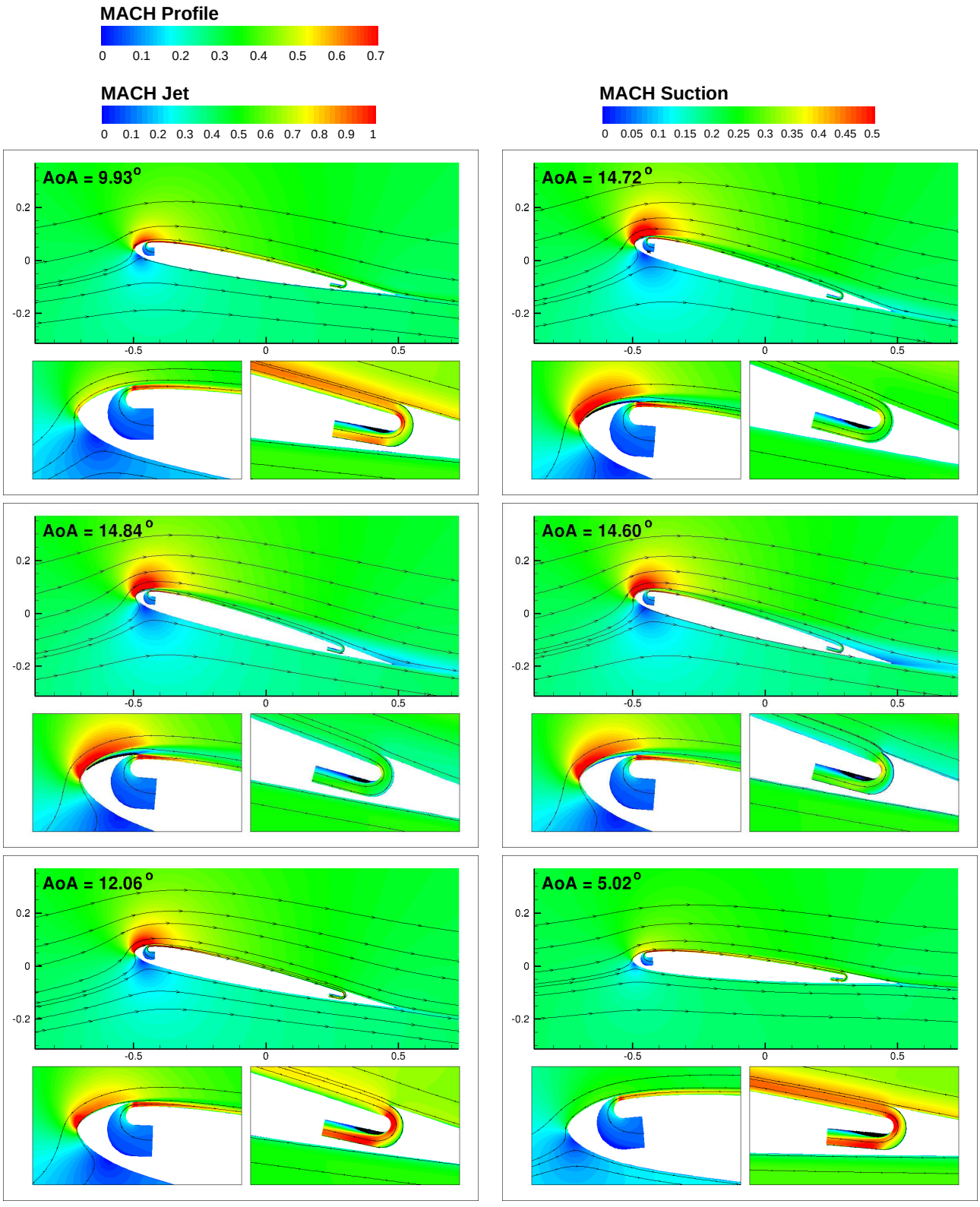

Figure 7: Instantaneous Mach contour of the CFJ pitching airfoil at $C\mu = 0.08$ with streamlines at different AoA for the mild-stall case.

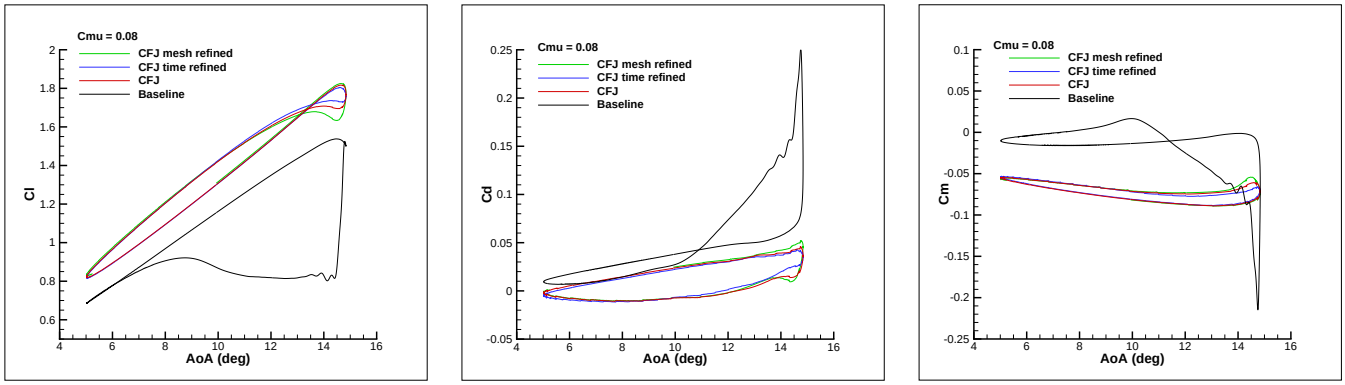

Figure 8: CFJ pitching airfoil C_l, C_d and C_m compared with Baseline calculation during mild-stall case.

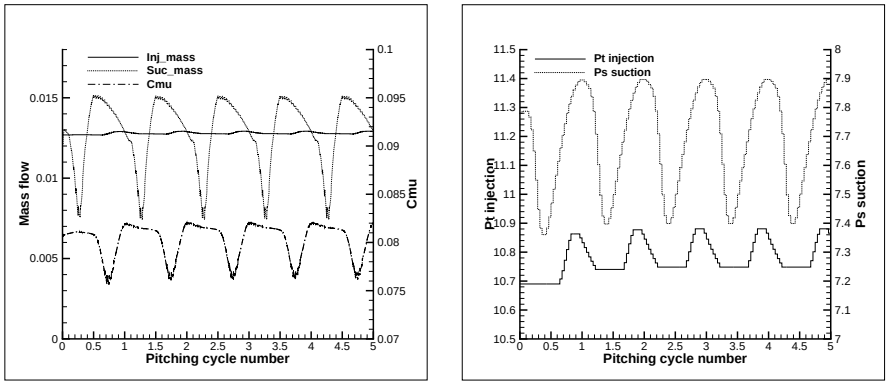

Figure 9: Evolution of injection mass flow, suction mass flow and $C\mu$ (top) and injection and suction pressure (bot) with the oscillation cycle for the mild-stall case.

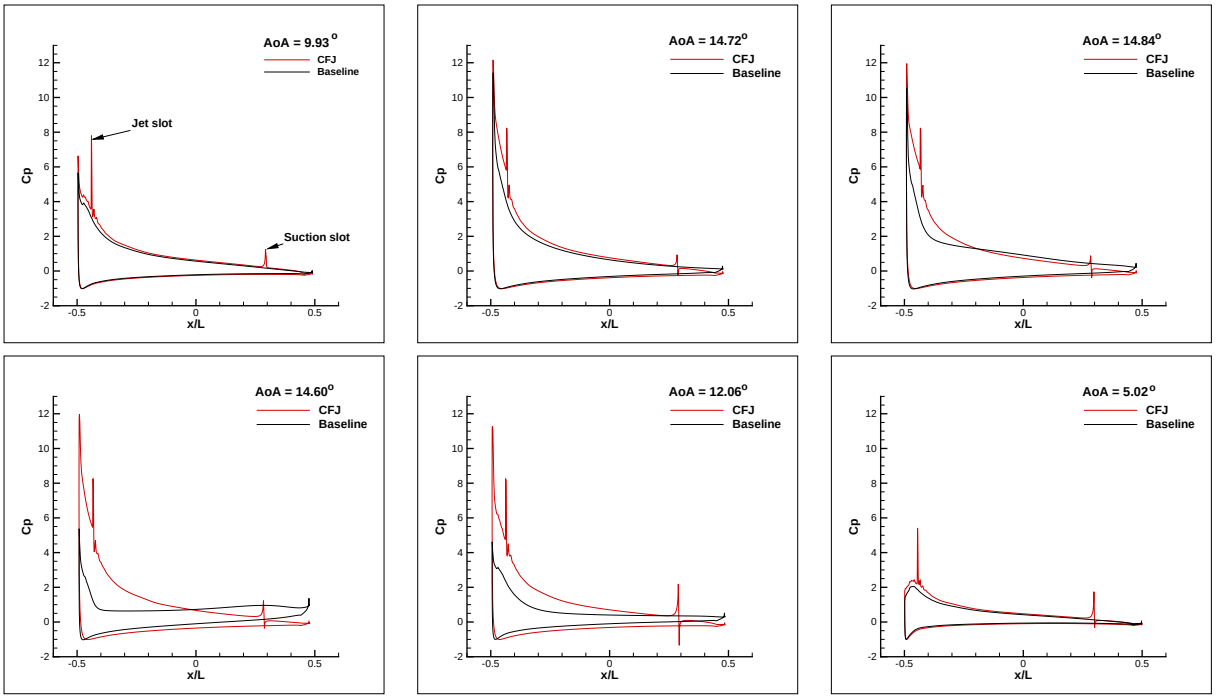

Figure 10: Numerically obtained pressure coefficient comparison between CFJ pitching airfoil and baseline pitching airfoil for the mild-stall case.

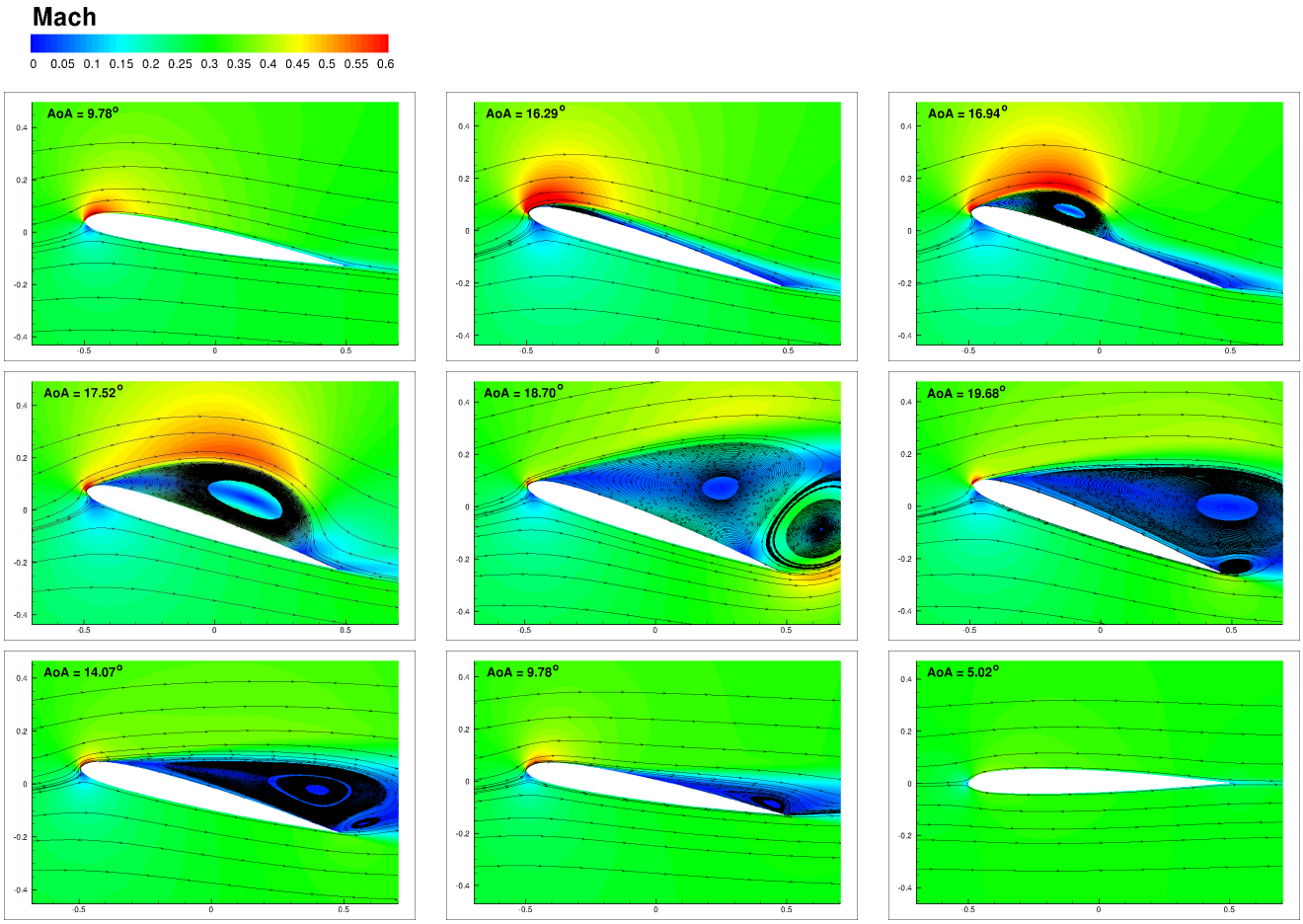

Figure 11: Instantaneous Mach contour of the baseline pitching airfoil with streamlines at different AoA for the deep-stall case.

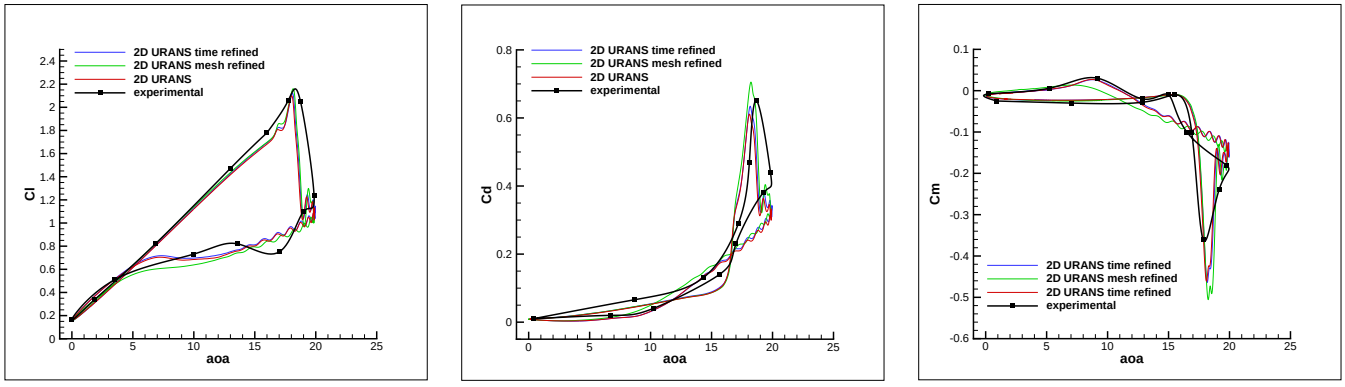

Figure 12: Baseline pitching airfoil C_l, C_d and C_m compared with experimental data during deep-stall case.

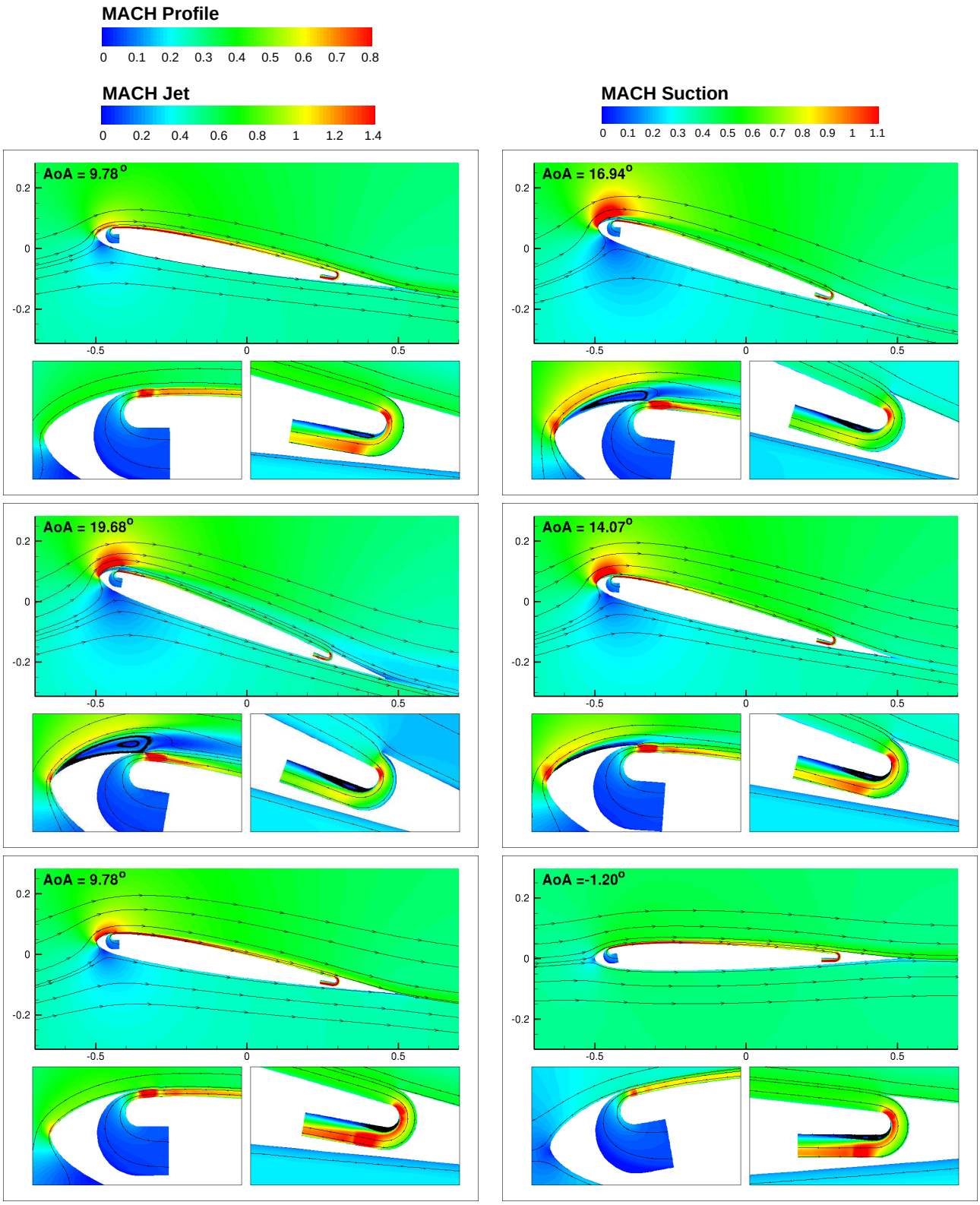

Figure 13: Instantaneous Mach contour of the CFJ pitching airfoil geometry 1 at $C\mu = 0.12$ with streamlines at different AoA for the deep-stall case.

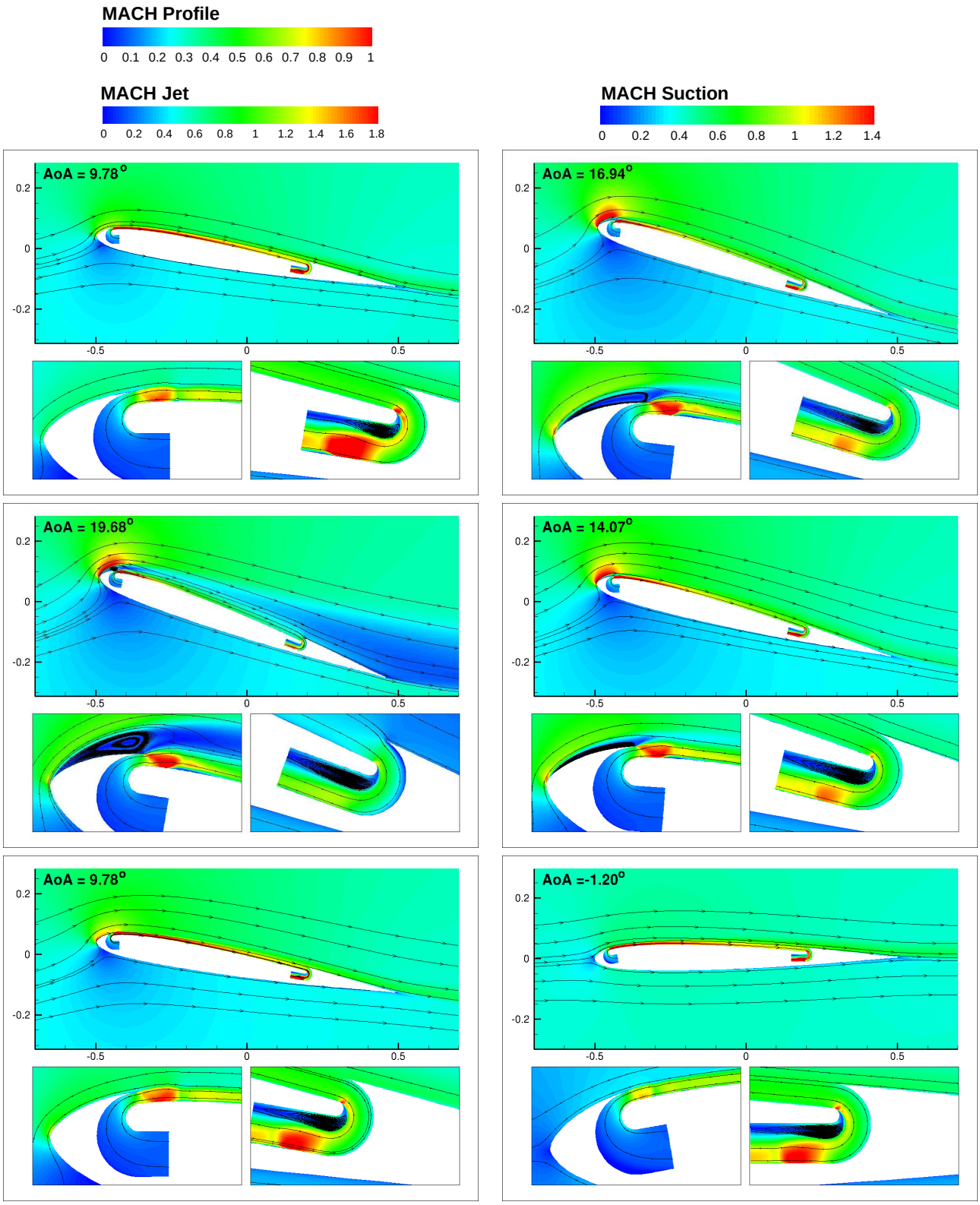

Figure 14: Instantaneous Mach contour of the CFJ pitching airfoil geometry 2 at $C\mu = 0.20$ with streamlines at different AoA for the deep-stall case.

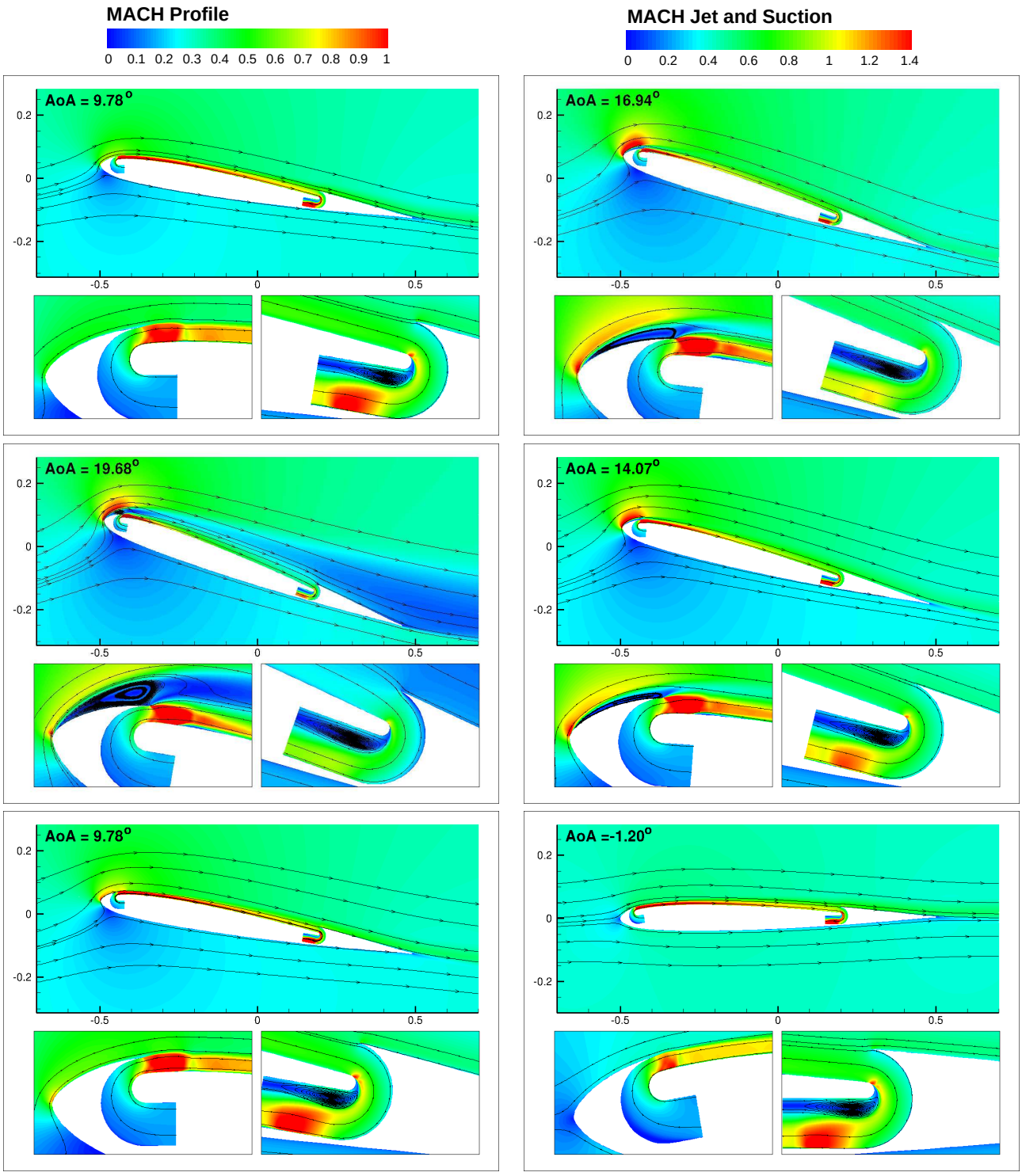

Figure 15: Instantaneous Mach contour of the CFJ pitching airfoil geometry 3 at $C\mu = 0.24$ with streamlines at different AoA for the deep-stall case.

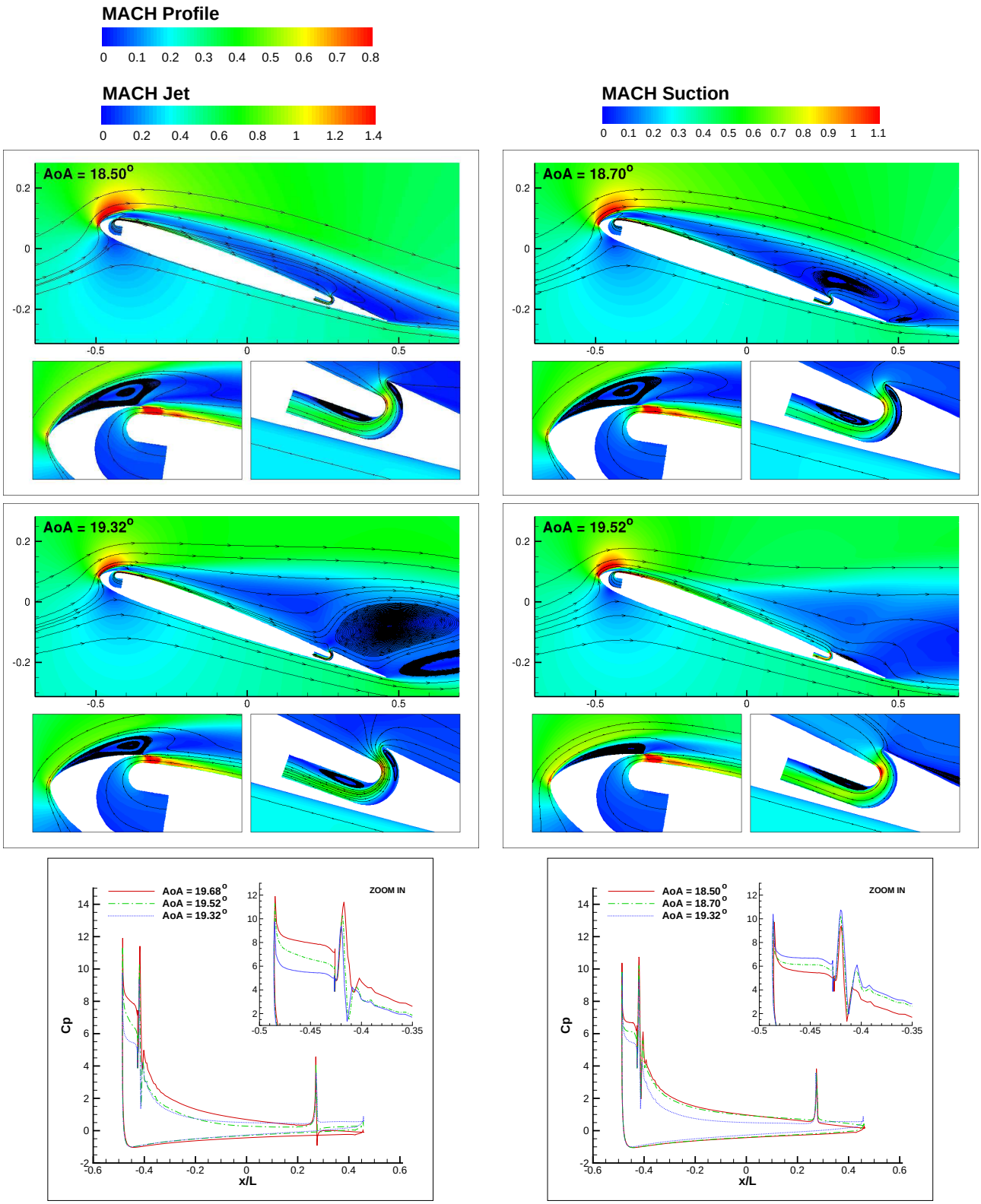

Figure 16: Dynamic-stall analysis using the instantaneous Mach contour and pressure coefficient of the CFJ pitching airfoil geometry 1 at $C\mu = 0.12$.

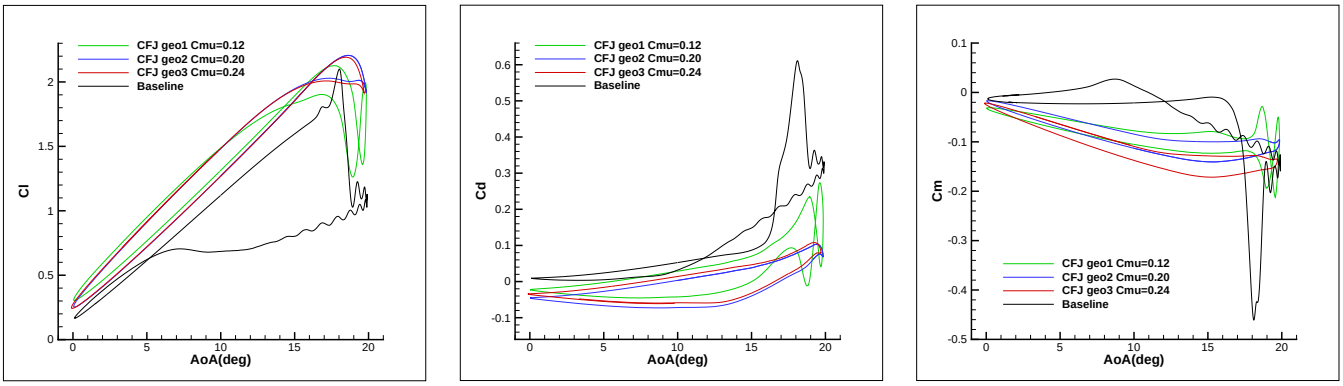

Figure 17: CFJ pitching airfoil C_l, C_d and C_m compared with Baseline calculation during deep-stall case.

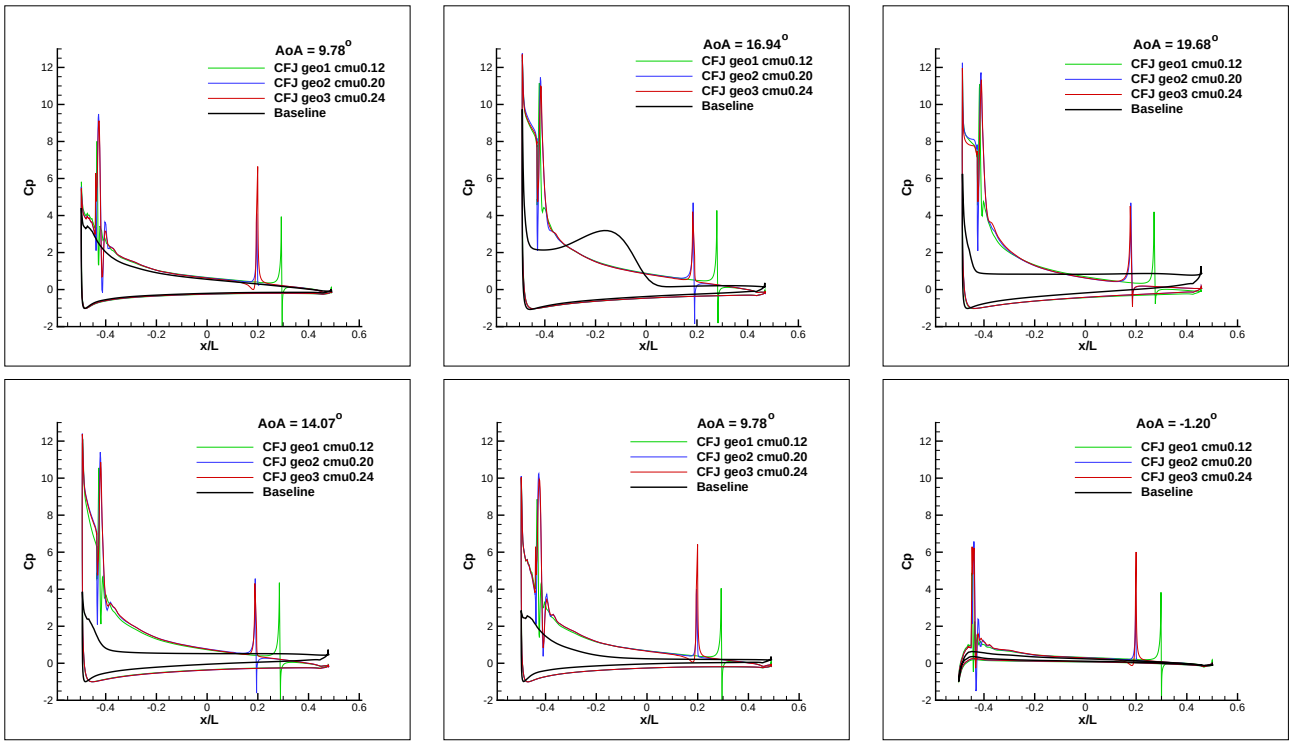

Figure 18: Numerically obtained pressure coefficient comparison between 3 CFJ pitching airfoil geometries and baseline pitching airfoil for the deep-stall case.

Case	$C\mu$	Cl_{ave}	Cd_{ave}	ΔCm	$(L/D)_{ave}$
No-stall baseline	X	0.51	0.027	0.05	19.2
Mild-stall baseline	X	1.01	0.053	0.23	19.1
Deep-stall baseline	X	0.78	0.114	0.49	6.8
No-stall CFJ geo1	0.08	0.87	0.018	0.10	48.9
Mild-stall CFJ geo1	0.08	1.33	0.011	0.04	118.3
Deep-stall CFJ geo1	0.12	1.23	0.031	0.18	39.9
Deep-stall CFJ geo2	0.20	1.28	-0.008	0.12	-156.0
Deep-stall CFJ geo3	0.24	1.27	7E-4	0.15	1844.4

Table 3: Summary of the aerodynamic performance for all the cases studied. The $(L/D)_{ave}$ consider only the aerodynamic forces applied on the airfoil and not the pumping power.